ELASTOPLASTIC ANALYSIS OF MISES METAL BY RETURN-MAPPING ALGORITHM FOR EXTENDED SUBLOADING SURFACE MODEL

TAKUYA. ANJIKI*, OKA. MASANORI* AND KOICHI. HASHIGUCHI†

* Yanmar Co. Ltd., Research and Development Center
2481 Umegahara, Maibara-shi, Shiga 521-8511, Japan
e-mail: takuya_anjiki@yanmar.com, web page: https://www.yanmar.com/global/

† MSC software Co. Ltd
Shinjuku First West 8th Floor ,1-23-7 Nishishinjuku, Shinjuku-ku, Tokyo 160-0023, Japan
Email: hashikoi87@gmail.com - Web page: http://www.mscsoftware.com/

Key words: Finite Element Method, Return-mapping, Subloading Surface Model, Consistent Tangent Modulus Tensor, Metal

Abstract. The extended subloading surface model is capable of representing not only monotonic but also cyclic loading behaviors accurately. The various return-mapping methods have been adopted to for the elastoplastic deformation analysis in FEM incorporating the subloading surface model. However, the past algorithms based on the expansion of the subloading surface is inapplicable to the cyclic loading behaviors. Then, the rigorous complete integration algorithm for Mises metal is adopted in this study. Additionally, it is implemented into the FEM software ABAQUS through the user-subroutine UMAT. The numerical calculations are performed for the forward and inverse loading processes by use of the proposed and the past implicit algorithms. A more accurate elastoplastic deformation analyses can be conducted by the proposed algorithm. Thus, it may be stated that the accurate numerical solution can be attained by adopting the proposed return-mapping algorithm for the general loading process.

1 INTRODUCTION

The subloading surface model does not incorporate the yield surface enclosing a purely-elastic domain. Instead, it is based on the natural postulate that the plastic strain rate develops as the stress approaches the yield surface [1, 2]. Therein, the subloading surface is incorporated, which passes through always the current stress point and keeps the similarity to the yield surface (the normal-yield surface). Therefore, the smooth transition from the elastic to the plastic state leading to the description of the continuous tangential modulus represents always in the subloading surface model. Moreover, the subloading surface model is capable of describing not only monotonic but also cyclic loading behaviors accurately.

The implicit stress integration algorithm based on the return-mapping for the subloading surface model in Mises metal has been studied in various approaches [3-7]. These loading criteria are based on the premise that the plastic strain rate is occurred by the expansion of the

subloading surface. Thus, these are limited to the description of monotonic loading behaviors and are unsuitable to the cyclic loading behaviors. In fact, the plastic strain rate is induced even when the subloading surface contracts in the elastic trial step if it once contracts but expands thereafter.

The return-mapping algorithm for the extended subloading surface model is formulated by incorporating the rigorous loading criterion in this study. It is capable of describing elastoplastic deformation in the general loading process involving not only monotonic but also cyclic loading for the Mises metals. Moreover, it has been implemented in the FEM software ABAQUS through the user-subroutine UMAT. Numerical analyses were performed not only for the forward loading but also the inverse loading in the multi-axial loading. In addition, the numerical calculations were performed by use of the past loading criterion in order to verify the necessity of the incorporation of the rigorous loading criterion.

2 EXTENDED SUBLOADING SURFACE MODEL

The constitutive equations in the extended subloading surface model [8] are addressed. The infinitesimal strain theory is adopted and the infinitesimal strain $\boldsymbol{\varepsilon}$ is additively decomposed into the elastic strain $\boldsymbol{\varepsilon}^e$ and the plastic strain $\boldsymbol{\varepsilon}^p$. The Cauchy stress $\boldsymbol{\sigma}$ is given by as following equation using Hooke's law with the elastic mudulus tensor $\mathbf{E}$.

$$\boldsymbol{\varepsilon} = \boldsymbol{\varepsilon}^e + \boldsymbol{\varepsilon}^p \tag{1}$$

$$\boldsymbol{\sigma} = \mathbf{E} : \boldsymbol{\varepsilon}^e = \mathbf{E} : \left(\boldsymbol{\varepsilon} - \boldsymbol{\varepsilon}^p \right) \tag{2}$$

The normal-yield surface for Mises metal is adopted. The subloading surface, which is similar to the normal-yield surface and passes though the current stress point, is given (Figure 1).

$$f\left(\hat{\boldsymbol{\sigma}}\right) = F\left(H\right) \tag{3}$$

$$f\left(\bar{\boldsymbol{\sigma}}\right) = RF\left(H\right), \quad f\left(\bar{\boldsymbol{\sigma}}\right) = \sqrt{\frac{3}{2}} \left\| \bar{\boldsymbol{\sigma}}' \right\| \tag{4}$$

The following relations hold in the variables for the normal-yield surface and subloading surface.

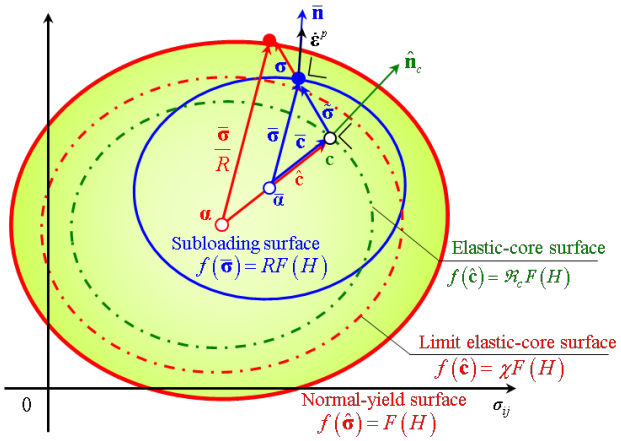

Figure 1: Normal-yield, subloading, and elastic-core surfaces.

$$\hat{\boldsymbol{\sigma}} \equiv \boldsymbol{\sigma} - \boldsymbol{\alpha},\ \bar{\boldsymbol{\sigma}} \equiv \boldsymbol{\sigma} - \bar{\boldsymbol{\alpha}},\ \hat{\mathbf{c}} \equiv \mathbf{c} - \boldsymbol{\alpha},\ \tilde{\boldsymbol{\sigma}} \equiv \boldsymbol{\sigma} - \mathbf{c},\ \bar{\boldsymbol{\alpha}} = \mathbf{c} - R(\mathbf{c} - \boldsymbol{\alpha}) = \mathbf{c} - R\hat{\mathbf{c}} \tag{5}$$

Where $\boldsymbol{\alpha}$ is the kinematic hardening variable, $\mathbf{c}$ is the elastic-core, and $\bar{\boldsymbol{\alpha}}$ is the center of the subloading surface and the conjugate point to the kinematic hardening variable in the normal-yield surface. $R\ (0 \le R \le 1)$ is the normal-yield ratio denoting the ratio of the size of the subloading surface to that of the normal-yield surface. The subloading surface coincides with the normal-yield surface when R=1. By contrast, the subloading surface become a point when R=0. The following equation is the evolution rule for the normal-yield ratio. $R_e\ (0 \le R_e < 1)$ is the material constant expressing the normal-yield ratio in the limit of the purely-elastic domain.

$$\overset{\bullet}{R} = U(R) \| \overset{\bullet}{\boldsymbol{\varepsilon}}^p \| \text{ for } \overset{\bullet}{\boldsymbol{\varepsilon}}^p \neq \mathbf{0} \tag{6}$$

$$U(R) = u \cot\left(\frac{\pi}{2} \frac{\langle R - R_e \rangle}{1 - R_e} \right) \tag{7}$$

$$R = \frac{2}{\pi}(1 - R_e) \cos^{-1}\left\{ \cos\left(\frac{R_0 - R_e}{1 - R_e} \frac{\pi}{2} \right) \exp\left(-u \frac{\left\| \boldsymbol{\varepsilon}^p - \boldsymbol{\varepsilon}_0^p \right\|}{1 - R_e} \frac{\pi}{2} \right) \right\} + R_e \tag{8}$$

Where $(\overset{\bullet}{})$ denotes the material time derivative and $\langle\ \rangle$ is Macauley's bracket.

The elastic-core surface, which passes through the elastic-core and is similar to the normal-yield surface with respect to the kinematic hardening variable is introduced. $\mathfrak{R}_c\ (0 < \mathfrak{R}_c < 1)$ is the ratio of the size of the elastic-core surface to that of the normal-yield surface. The elastic-core limit surface is introduced to regulate the elastic-core to move only inside of it because it is inapplicable that the elastic-core coincides normal-yield surface.

$$f(\hat{\mathbf{c}}) = \mathfrak{R}_c F(H) \tag{9}$$

$$f(\hat{\mathbf{c}}) = \chi F(H) \tag{10}$$

Where $\chi\ (<1)$ is a material constant expressing the limit of the elastic-core surface.

The plastic strain rate is given by the associated flow rule and the normalized outward-normal vector of the subloading surface $\bar{\mathbf{n}}$.

$$\overset{\bullet}{\boldsymbol{\varepsilon}}^p = \overset{\bullet}{\lambda}\, \bar{\mathbf{n}},\ \bar{\mathbf{n}} \equiv \frac{\partial f(\bar{\boldsymbol{\sigma}})}{\partial \bar{\boldsymbol{\sigma}}} \Bigg/ \left\| \frac{\partial f(\bar{\boldsymbol{\sigma}})}{\partial \bar{\boldsymbol{\sigma}}} \right\| \tag{11}$$

Where $\dot{\lambda}\ (\ge 0)$ is the plastic multiplier. The evolution of the elastic-core, isotropic and kinematic hardening is given by the non-linear hardening rule.

$$\overset{\bullet}{\mathbf{c}} = \mathbf{s} \overset{\bullet}{\lambda} = C_c \left(\bar{\mathbf{n}} - \frac{\mathfrak{R}_c}{\chi} \hat{\mathbf{n}}_c \right) \overset{\bullet}{\lambda} \tag{12}$$

$$F(H) = F_0 \left\{ 1 + h_1 \left[1 - \exp(-h_2 H) \right] \right\},\ \overset{\bullet}{H} = \sqrt{\frac{2}{3}} \| \overset{\bullet}{\boldsymbol{\varepsilon}}^p \| \tag{13}$$

$$\overset{\bullet}{\boldsymbol{\alpha}} = \mathbf{a} \overset{\bullet}{\lambda} = a_\alpha \left(\bar{\mathbf{n}} - \sqrt{\frac{2}{3}} \frac{1}{r_\alpha F(H)} \boldsymbol{\alpha} \right) \overset{\bullet}{\lambda} \tag{14}$$

F_0 is the initial value for isotropic hardening function, and C_c, h_1, h_2, a_α and r_α are the material constants.

3 RETURN-MAPPING ALGORITHM

3.1 Rigorous loading criterion

The complete implicit stress integration algorithm based on the return-mapping is adopted, in which the strain increment $\Delta\boldsymbol{\varepsilon}_{n+1}$ inputs the elastic deformation in the elastic trial step [9]. The elastic trial stress $\boldsymbol{\sigma}_{n+1}^{\text{trial}}$ is calculated by the elastic equation using the elastic strain $\boldsymbol{\varepsilon}_n^e$ in step n and the strain increment, where, the subscript denotes the number of steps.

$$\boldsymbol{\sigma}_{n+1}^{\text{trial}} = \mathbf{E} : \left(\boldsymbol{\varepsilon}_n^e + \Delta\boldsymbol{\varepsilon}_{n+1}\right) \tag{15}$$

The following loading criterion has been adopted for the subloading surface model in the past [3-6].

$$\begin{cases} f\left(\boldsymbol{\sigma}_{n+1}^{\text{trial}} - \bar{\boldsymbol{\alpha}}_n\right) - R_n F\left(H_n\right) \le 0 \text{ or } f\left(\boldsymbol{\sigma}_{n+1}^{\text{trial}} - \bar{\boldsymbol{\alpha}}_n\right) - R_e F\left(H_n\right) \le 0 : \Delta\boldsymbol{\varepsilon}_{n+1}^p = \mathbf{0},\ \boldsymbol{\sigma}_{n+1} = \boldsymbol{\sigma}_{n+1}^{\text{trial}} \\ \text{Otherwise} \qquad : \Delta\boldsymbol{\varepsilon}_{n+1}^p \neq \mathbf{0},\ \boldsymbol{\sigma}_{n+1} \neq \boldsymbol{\sigma}_{n+1}^{\text{trial}} \end{cases} \tag{16}$$

The past loading criterion is based on the premise that the elastic trial stress goes out for the plastic loading process from the subloading surface and the purely-elastic domain in the step n. In fact, however, the plastic strain rate is induced even when the subloading surface contracts in the elastic trial step if it once contracts but expands thereafter. In order to explain this fact concisely, the example of inverse monotonic loading process is shown in Figure 2. The elastic trial stress is directed toward the interior of the current subloading surface, and the subloading surface in elastic trial step once contracts. However, it re-expands larger than purely-elastic domain. Therefore, this elastic trial step is the plastic loading process which the elastic trial stress goes out from the subloading surface and the purely-elastic domain. It is necessary to occur the plastic strain rate even when subloading surface contracts in the elastic trial step if it once contracts but expands thereafter. However, the past loading criterion can't consider this fact and is inapplicable to describe of cyclic loading behaviors.

The numerical errors using the past loading criterion can be prevented by setting the input increment to be sufficiently small. However, the advantage of highly accurate and efficient calculation in return-mapping is not performed. Then, the rigorous loading criterion is adopted in this study. In the rigorous loading criterion, it formulated based on the fact in Figure 3.

(1) When the elastic trial stress increment $\Delta\boldsymbol{\sigma}_{n+1}^{\text{trial}} = \boldsymbol{\sigma}_{n+1}^{\text{trial}} - \boldsymbol{\sigma}_n$ goes out from the subloading surface and the purely-elastic domain in the step n, the plastic strain rate is induced.

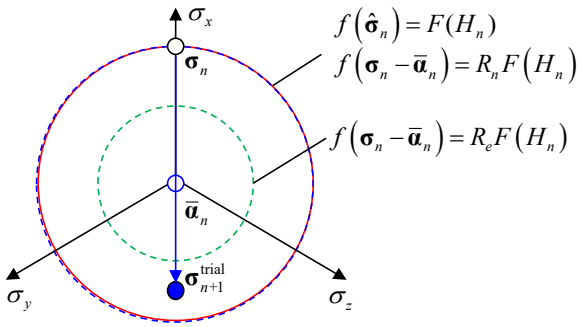

Figure 2: Inverse loading process: the subloading surface in elastic trial step re-expand after once contraction.

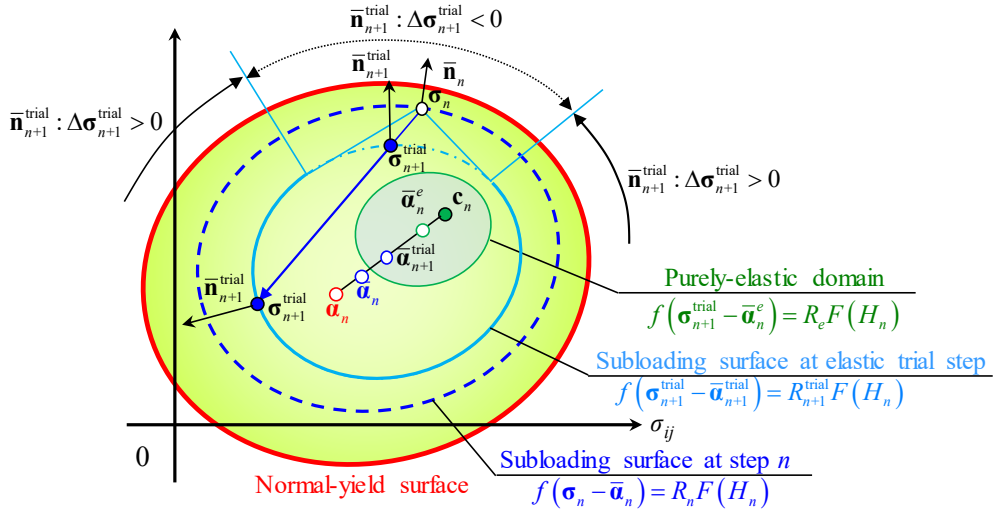

Figure 3: Rigorous loading criterion for exetnded subloading surface model.

(2) When the elastic trial stress increment $\Delta\boldsymbol{\sigma}_{n+1}^{\text{trial}}$ goes in for an inverse loading process the subloading surface in the step n ($\bar{\mathbf{n}}_n:\Delta\boldsymbol{\sigma}_{n+1}^{\text{trial}}<0$). The plastic strain rate is induced even when the subloading surface contracts in the elastic trial step if it once contracts but expands thereafter. In this case elastic trial stress increment and outward-normal vector of the subloading surface in the elastic trial step ($\bar{\mathbf{n}}_{n+1}^{\text{trial}}:\Delta\boldsymbol{\sigma}_{n+1}^{\text{trial}}>0$) forms an acute angle ($\theta\le 90°$). However, the plastic strain rate is not induced when the elastic trial stress $\boldsymbol{\sigma}_{n+1}^{\text{trial}}$ is inside the purely-elastic domain ($f(\bar{\boldsymbol{\sigma}}_{n+1}^{\text{trial}}-\bar{\boldsymbol{\alpha}}_n^e)-R_eF(H_n)<0$).

Thus, the following loading equations are introduced as the rigorous loading criterion.

(1) $\bar{\mathbf{n}}_{n+1}^{\text{trial}}:\Delta\boldsymbol{\sigma}_{n+1}^{\text{trial}}\ge 0$ (Forward loading)

$$\begin{cases}\text{(i)}\ f(\boldsymbol{\sigma}_{n+1}^{\text{trial}}-\bar{\boldsymbol{\alpha}}_n^e)-R_eF(H_n)\le 0\ :\Delta\boldsymbol{\varepsilon}_{n+1}^p=\mathbf{0},\quad \boldsymbol{\sigma}_{n+1}=\boldsymbol{\sigma}_{n+1}^{\text{trial}}\\ \text{(ii)}\ f(\boldsymbol{\sigma}_{n+1}^{\text{trial}}-\bar{\boldsymbol{\alpha}}_n^e)-R_eF(H_n)>0\ :\Delta\boldsymbol{\varepsilon}_{n+1}^p\ne\mathbf{0}\end{cases}$$

(2) Otherwise ($\bar{\mathbf{n}}_n:\Delta\boldsymbol{\sigma}_{n+1}^{\text{trial}}<0$) (Inverse loading)

$$\begin{cases}\text{(i)}\ \bar{\mathbf{n}}_{n+1}^{\text{trial}}:\Delta\boldsymbol{\sigma}_{n+1}^{\text{trial}}\le 0:\Delta\boldsymbol{\varepsilon}_{n+1}^p=\mathbf{0},\quad \boldsymbol{\sigma}_{n+1}=\boldsymbol{\sigma}_{n+1}^{\text{trial}}\\ \text{(ii)}\ \text{Otherwise}\ (\bar{\mathbf{n}}_{n+1}^{\text{trial}}:\Delta\boldsymbol{\sigma}_{n+1}^{\text{trial}}>0)\begin{cases}\text{(a)}\ f(\boldsymbol{\sigma}_{n+1}^{\text{trial}}-\bar{\boldsymbol{\alpha}}_n^e)-R_eF(H_n)\le 0:\\ \quad\Delta\boldsymbol{\varepsilon}_{n+1}^p=\mathbf{0},\quad \boldsymbol{\sigma}_{n+1}=\boldsymbol{\sigma}_{n+1}^{\text{trial}}\\ \text{(b)}\ f(\boldsymbol{\sigma}_{n+1}^{\text{trial}}-\bar{\boldsymbol{\alpha}}_n^e)-R_eF(H_n)>0:\\ \quad\Delta\boldsymbol{\varepsilon}_{n+1}^p\ne\mathbf{0}\end{cases}\end{cases}\tag{17}$$

Where, the variables for the loading criterion are expressed by

$$\Delta\boldsymbol{\sigma}_{n+1}^{\text{trial}}=\boldsymbol{\sigma}_{n+1}^{\text{trial}}-\boldsymbol{\sigma}_n\tag{18}$$

$$\bar{\boldsymbol{\alpha}}_{n+1}^{\text{trial}}=\mathbf{c}_n-R_{n+1}^{\text{trial}}\hat{\mathbf{c}}_n,\quad \bar{\boldsymbol{\alpha}}_{n+1}^e=\mathbf{c}_n-R_e\hat{\mathbf{c}}_n\tag{19}$$

$$\bar{\boldsymbol{\sigma}}_n=\boldsymbol{\sigma}_n-\bar{\boldsymbol{\alpha}}_n=\tilde{\boldsymbol{\sigma}}_n+R_n\hat{\mathbf{c}}_n,\quad \bar{\boldsymbol{\sigma}}_{n+1}^{\text{trial}}=\boldsymbol{\sigma}_{n+1}^{\text{trial}}-\bar{\boldsymbol{\alpha}}_{n+1}^{\text{trial}}=\tilde{\boldsymbol{\sigma}}_{n+1}^{\text{trial}}+R_{n+1}^{\text{trial}}\hat{\mathbf{c}}_n\tag{20}$$

$$\bar{\mathbf{n}}_n\equiv\frac{\partial f\left(\bar{\boldsymbol{\sigma}}_n\right)}{\partial\bar{\boldsymbol{\sigma}}_n}\Bigg/\left\|\frac{\partial f\left(\bar{\boldsymbol{\sigma}}_n\right)}{\partial\bar{\boldsymbol{\sigma}}_n}\right\|,\quad \bar{\mathbf{n}}_{n+1}^{\text{trial}}\equiv\frac{\partial f\left(\bar{\boldsymbol{\sigma}}_{n+1}^{\text{trial}}\right)}{\partial\bar{\boldsymbol{\sigma}}_{n+1}^{\text{trial}}}\Bigg/\left\|\frac{\partial f\left(\bar{\boldsymbol{\sigma}}_{n+1}^{\text{trial}}\right)}{\partial\bar{\boldsymbol{\sigma}}_{n+1}^{\text{trial}}}\right\|\tag{21}$$

The subloading surface function in the elastic trial step is expressed by the elastic trial stress and the normal-yield ratio at the elastic trial stress R_{n+1}^{trial}. Additionally, the normal-yield ratio in the elastic trial step is expressed by

$$\sqrt{\frac{3}{2}}\left\|\overline{\boldsymbol{\sigma}}_{n+1}^{\text{trial}\prime}\right\| = R_{n+1}^{\text{trial}} F(H_n) \tag{22}$$

$$R_{n+1}^{\text{trial}} = \frac{\tilde{\boldsymbol{\sigma}}_{n+1}^{\text{trial}\prime} : \hat{\mathbf{c}}_n' + \sqrt{\left(\tilde{\boldsymbol{\sigma}}_{n+1}^{\text{trial}\prime} : \hat{\mathbf{c}}_n'\right)^2 + \left[\frac{2}{3}\left(F(H_n)\right)^2 - \left\|\hat{\mathbf{c}}_n'\right\|^2\right]\left\|\tilde{\boldsymbol{\sigma}}_{n+1}^{\text{trial}\prime}\right\|^2}}{\frac{2}{3}\left(F(H_n)\right)^2 - \left\|\hat{\mathbf{c}}_n'\right\|^2} \tag{23}$$

3.2 Plastic corrector process

In the return-mapping algorithm, the elastic trial stress is adopted as updated stress when it is judged as an elastic loading process by the loading criterion. By contrast, when the elastic trial stress is judged as a plastic loading process, the plastic corrector process is applied to calculate the stress and state variables after the plastic deformation. The equilibrium equations to correct stress and state variables by an iterative convergence calculation are expressed by

$$\begin{aligned}
\mathbf{Y}_\sigma &\equiv \mathbf{E}^{-1} : \boldsymbol{\sigma}_{n+1} - \boldsymbol{\varepsilon}_{n+1}^{e\,\text{trial}} + \Delta\lambda_{n+1}\overline{\mathbf{n}}_{n+1} \\
\mathbf{Y}_\alpha &\equiv \boldsymbol{\alpha}_{n+1} - \boldsymbol{\alpha}_n - \mathbf{a}_{n+1}\Delta\lambda_{n+1} \\
\mathbf{Y}_c &\equiv \mathbf{c}_{n+1} - \mathbf{c}_n - \mathbf{s}_{n+1}\Delta\lambda_{n+1} \\
Y_H &\equiv H_{n+1} - H_n - \sqrt{\frac{2}{3}}\Delta\lambda_{n+1} \\
Y_S &\equiv f\left(\overline{\boldsymbol{\sigma}}_{n+1}\right) - R_{n+1}F(H_{n+1})
\end{aligned} \tag{24}$$

Where, the unknown vector $\mathbf{X}$ and the residual vector $\mathbf{Y}(\mathbf{X})$ are introduced.

$$\mathbf{X} \equiv \left(\boldsymbol{\sigma}_{n+1} \quad \boldsymbol{\alpha}_{n+1} \quad \mathbf{c}_{n+1} \quad H_{n+1} \quad \Delta\lambda_{n+1}\right)^T \tag{25}$$

$$\mathbf{Y}(\mathbf{X}) \equiv \left(\mathbf{Y}_\sigma \quad \mathbf{Y}_\alpha \quad \mathbf{Y}_c \quad Y_H \quad Y_S\right)^T = \mathbf{0} \tag{26}$$

Additionally, the initial values of the unknown vector variables and the normal-yield ratio are expressed by the following equations.

$$\boldsymbol{\varepsilon}_{n+1}^{e(0)} = \boldsymbol{\varepsilon}_{n+1}^{e\,\text{trial}},\ \boldsymbol{\alpha}_{n+1}^{(0)} = \boldsymbol{\alpha}_n,\ \mathbf{c}_{n+1}^{(0)} = \mathbf{c}_n,\ H_{n+1}^{(0)} = H_n,\ \Delta\lambda_{n+1}^{(0)} = 0 \tag{27}$$

$$\begin{aligned}
R_n \geq R_e &: R_{n+1}^{(0)} = R_{\text{n}} \\
R_n < R_e &: R_{n+1}^{(0)} = R_e
\end{aligned} \tag{28}$$

Where, the superscripts indicate the number of iterations in the convergence calculation.

Equation (26) is expressed by the primary approximation of the Taylor expansion. The unknown vectors are updated from iteration k to k+1 of the convergence calculation using the Jacobi matrix. Each element of the Jacobi matrix is introduced by a direct partial differential operation, but description of that is omitted in this article.

$$\mathbf{Y}\left(\mathbf{X}^{(k+1)}\right) \cong \mathbf{Y}\left(\mathbf{X}^{(k)}\right) + \mathbf{J}\left(\mathbf{X}^{(k)}\right)\cdot \mathrm{d}\mathbf{X} = \mathbf{0} \tag{29}$$

$$\mathbf{X}^{(k+1)} = \mathbf{X}^{(k)} + \mathbf{d}\mathbf{X}^{(k)} = \mathbf{X}^{(k)} - \left[\mathbf{J}\left(\mathbf{X}^{(k)}\right)\right]^{-1}\mathbf{Y}\left(\mathbf{X}^{(k)}\right) \tag{30}$$

$$\left\| \mathbf{Y}\left(\mathbf{X}^{(k)}\right) \right\| < 1.0\times10^{-6} \tag{31}$$

The convergence calculation of the plastic corrector process continues until it satisfies the criterion expressed by Equation (31). Although they include vectors with various units, the stress dimensional vector controlling the iterative calculation converges sufficiently when the convergence criterion is satisfied.

Moreover, the consistent tangent modulus tensor is adopted to efficiently satisfy the global equilibrium condition in the static FEM analysis. In this study, it was introduced using a numerical procedure using the perturbation strain [10]. The perturbation strain was setted $\Delta\varepsilon = 10\times10^{-8}$ in this study.

3.3 Initial value for normal-yield ratio in plastic corrector process

The plastic strain rate is induced even when the subloading surface contracts in the elastic trial step if it once contracts but expands larger than purely-elastic domain thereafter (Equation (17) (2) (ii) (b)). There are various stress directions in this case. However, in fact, among them are the loading processes in which the subloading surface in the elastic trial step re-expands after temporary contraction without passing the purely-elastic domain (Figure 4). In this case, Equation (28) may induce numerical error and can't adequately express the general loading process. Then, the initial value for the normal-yield ratio in the plastic corrector process has to be applied it at the transition point where the subloading surface switches from contraction to re-expansion. The calculation method for the normal-yield ratio at the transition point was introduced.

The subloading surface state in the transition point where the subloading surface switches from contraction to re-expansion is shown in Figure 5. The stress $\boldsymbol{\sigma}_{n+1}^{0}$ and normal-yield ratio R_{n+1}^{0} at the transition point must satisfy

$$f\left(\bar{\boldsymbol{\sigma}}_{n+1}^{0}\right) = R_{n+1}^{0}F\left(H_n\right) \tag{32}$$

Moreover, the elastic trial stress tangents to the subloading surface at the transition point. Therefore, the elastic trial stress and the outward-normal vector $\bar{\mathbf{n}}_{n+1}^{0}$ of the subloading surface are intersected at right angles at the transition point. The stress at the transition point is given by the following equation based on the relationship between the stress at current step and the elastic trial stress.

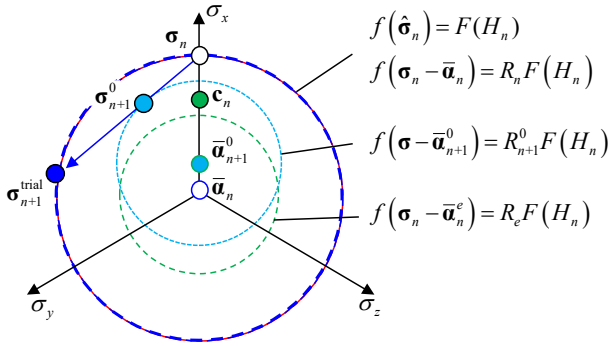

Figure 4: Inverse loading process which the elastic trial stress contracts and re-expands without passing the purely-elastic domain.

$$\bar{\mathbf{n}}^0_{n+1} : \Delta\boldsymbol{\sigma}^{\text{trial}}_{n+1} = 0 \tag{33}$$

$$\boldsymbol{\sigma}^0_{n+1} \equiv c\Delta\boldsymbol{\sigma}^{\text{trial}}_{n+1} + \boldsymbol{\sigma}_n \quad (0 \le c \le 1) \tag{34}$$

Where, c is a scalar variable satisfied by Equation (32), (33) and $0 \le c \le 1$. Additionally, the variables of the subloading surface at the transition point are expressed by

$$\bar{\boldsymbol{\sigma}}^0_{n+1} \equiv \boldsymbol{\sigma}^0_{n+1} - \bar{\boldsymbol{\alpha}}^0_{n+1} = c\Delta\boldsymbol{\sigma}^{\text{trial}}_{n+1} + \tilde{\boldsymbol{\sigma}}_n + R^0_{n+1}\hat{\mathbf{c}}_n \ , \ \bar{\boldsymbol{\alpha}}^0_{n+1} \equiv \mathbf{c}_n - R^0_{n+1}\hat{\mathbf{c}}_n \tag{35}$$

$$\bar{\mathbf{n}}^0_{n+1} \equiv \frac{\partial f\left(\bar{\boldsymbol{\sigma}}^0_{n+1}\right)}{\partial \bar{\boldsymbol{\sigma}}^0_{n+1}} \Bigg/ \left\| \frac{\partial f\left(\bar{\boldsymbol{\sigma}}^0_{n+1}\right)}{\partial \bar{\boldsymbol{\sigma}}^0_{n+1}} \right\| \tag{36}$$

The normal-yield ratio and scalar variable c at the transition point are expressed by

$$\sqrt{\frac{3}{2}} \left\| c\Delta\boldsymbol{\sigma}^{\text{trial}'}_{n+1} + \tilde{\boldsymbol{\sigma}}'_n + R^0_{n+1}\hat{\mathbf{c}}'_n \right\| = R^0_{n+1} F\left(H_n\right) \tag{37}$$

$$\left(c\Delta\boldsymbol{\sigma}^{\text{trial}'}_{n+1} + \tilde{\boldsymbol{\sigma}}'_n + R^0_{n+1}\hat{\mathbf{c}}'_n\right) : \Delta\boldsymbol{\sigma}^{\text{trial}}_{n+1} = 0 \tag{38}$$

The scalar variable c is obtained by solving the Equation (37) and (38).

$$\Delta\boldsymbol{\sigma}^{\text{trial}'}_{n+1} : \Delta\boldsymbol{\sigma}^{\text{trial}'}_{n+1} c^2 + 2\Delta\boldsymbol{\sigma}^{\text{trial}'}_{n+1} : \left(\tilde{\boldsymbol{\sigma}}'_n + R^0_{n+1}\hat{\mathbf{c}}'_n\right) c + \left(\tilde{\boldsymbol{\sigma}}'_n + R^0_{n+1}\hat{\mathbf{c}}'_n\right) : \left(\tilde{\boldsymbol{\sigma}}'_n + R^0_{n+1}\hat{\mathbf{c}}'_n\right) - \frac{2}{3}\left(R^0_{n+1}F\left(H_n\right)\right)^2 = 0 \tag{39}$$

$$c = \frac{-S_{sc} - R^0_{n+1}S_{sa} + \sqrt{\left(S_{sc} + R^0_{n+1}S_{sa}\right)^2 - S_{ss}\left[\left(\tilde{\boldsymbol{\sigma}}'_n + R^0_{n+1}\hat{\mathbf{c}}'_n\right) : \left(\tilde{\boldsymbol{\sigma}}'_n + R^0_{n+1}\hat{\mathbf{c}}'_n\right) - \frac{2}{3}\left(R^0_{n+1}F\left(H_n\right)\right)^2\right]}}{S_{ss}} \tag{40}$$

$$S_{ss} = \Delta\boldsymbol{\sigma}^{\text{trial}'}_{n+1} : \Delta\boldsymbol{\sigma}^{\text{trial}'}_{n+1}, \ S_{sa} = \Delta\boldsymbol{\sigma}^{\text{trial}'}_{n+1} : \hat{\mathbf{c}}'_n, \ S_{sc} = \Delta\boldsymbol{\sigma}^{\text{trial}'}_{n+1} : \tilde{\boldsymbol{\sigma}}'_n \tag{41}$$

Moreover, the normal-yield ratio at the transition point is expressed by substituting the scalar variable c to Equation (38).

$$\left(S_{sc} + R^0_{n+1}S_{sa}\right)^2 - S_{ss}\left[\left(\tilde{\boldsymbol{\sigma}}'_n + R^0_{n+1}\hat{\mathbf{c}}'_n\right) : \left(\tilde{\boldsymbol{\sigma}}'_n + R^0_{n+1}\hat{\mathbf{c}}'_n\right) - \frac{3}{2}\left(R^0_{n+1}F\left(H_n\right)\right)^2\right] = 0 \tag{42}$$

$$R^0_{\text{n+1}} = \frac{-S_{sc}S_{sa} + S_{ss}S_{ca} + \sqrt{\left(S_{sc}S_{sa} - S_{ss}S_{ca}\right)^2 - \left[S_{sa}{}^2 - S_{ss}S_{aa} - \frac{3}{2}F\left(H_n\right)^2\right]\left(S_{sc}{}^2 - S_{ss}S_{cc}\right)}}{S_{sc}{}^2 - S_{ss}S_{cc}} \tag{43}$$

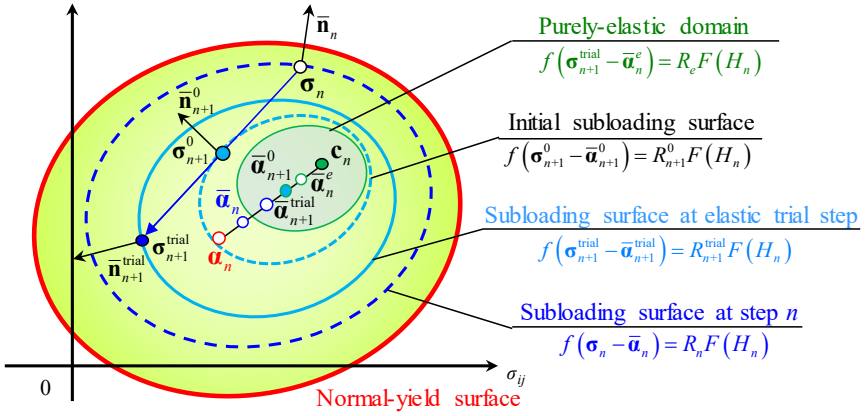

Figure 5: Rigorous calculation method for initial value of normal-yield ratio in the plastic corrector process.

$$S_{ca} = \tilde{\boldsymbol{\sigma}}'_n : \hat{\mathbf{c}}'_n,\ S_{aa} = \hat{\mathbf{c}}'_n : \hat{\mathbf{c}}'_n,\ S_{cc} = \tilde{\boldsymbol{\sigma}}'_n : \tilde{\boldsymbol{\sigma}}'_n \tag{44}$$

4 NUMRRICAL VERIFICATION

The proposed formulations were implemented in the FEM software ABAQUS through the user subroutine UMAT. The numerical analyses applied elastoplastic deformation using single-element model with the primary hexahedral element. Additionally, we verified the accuracy of the implicit stress integration algorithm based on the rigorous and past loading criteria. The material constants for the numerical analyses are shown in Table. 1. Concisely, the isotropic and kinematic hardening are not discussed in this study.

Table 1: Material constatants

Elastic property		Translation of elastic-core		Evolution of normal-yield ratio			Yield stress
E [GPa]	ν	C_c [MPa]	χ	R_e	u_0	u_c	F_0 [MPa]
160	0.30	10000	0.60	0.3	80	2.0	500

4.1 Verification with single-element model

First, the uniaxial forward and inverse loading process was performed. The forward loading process was a deformation of up to 2% of the nominal strain in the X-axis direction, and the inverse loading process was a deformation of up to 0% in the nominal strain. Numerical analysis increment was performed by four steps per process.

Stress $\boldsymbol{\sigma}_a$ at the end of the forward loading process, elastic trial stress $\boldsymbol{\sigma}_b$ and the subloading surface state in the elastic trial step of the beginning of the inverse loading process are shown in Figure 6 (a). The stress-strain curves and elastic trial stress in the beginning of the inverse loading process are shown in Figure 6 (b, c). There were no difference in the stress-strain curves obtained by the rigorous and past loading criteria because the forward loading process was only expasion process of the subloading surface.

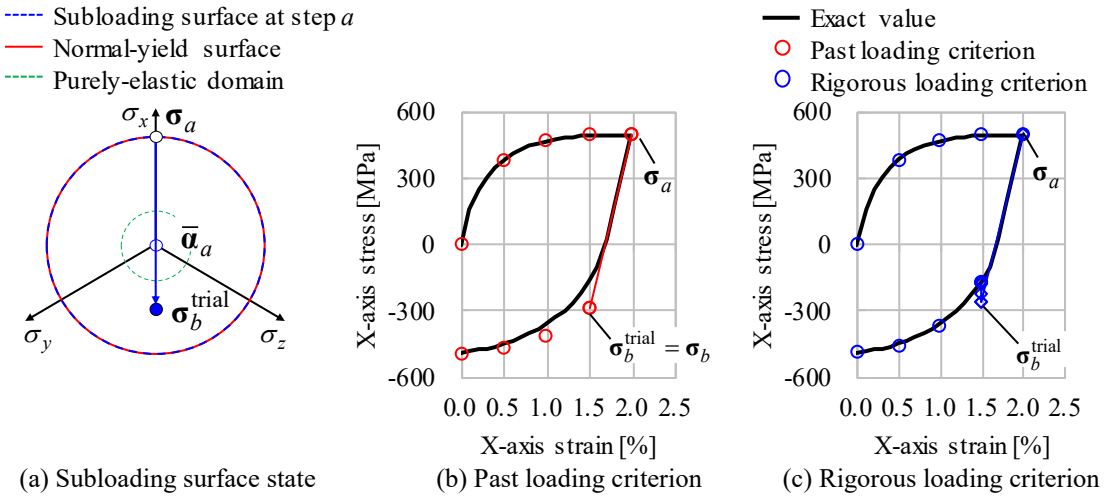

(a) Subloading surface state (b) Past loading criterion (c) Rigorous loading criterion

Figure 6: Uniaxial forward and inverse loading process, which the subloading surface in elastic trial step of beginning of inverse loading re-expand after once contraction.

In the beginning step of the inverse loading process, the subloading surface re-expanded larger than the purely-elastic domain after it once contracted less than that domain as was similar to Figure 2. In this case, the elastic trial stress $\boldsymbol{\sigma}_b^{\text{trial}}$ was judged as an elastic loading process by the past loading criterion, and the numerical value was calculated larger than exact value (Figure 6 (b)). On the contrary, the rigorous loading criterion judged as a plastic loading process. Thus, the plastic corrector step was applied and the elastic trial stress $\boldsymbol{\sigma}_b^{\text{trial}}$ was corrected to the subloading surface containing the plastic deformation (Figure 6 (c)).

Next, the bi-axial forward and inverse loading process was performed to verify the accuracy of the general-loading process. The forward loading process provided a deformation of up to 2% of the nominal strain in the X-axis direction. In inverse loading process, the displacement boundary conditions in the X-axis direction were removed and the stress produced in the forward loading process gradually decreased to 0 MPa. Additionally, the deformation that was induced in the Y-axis direction was restored to 0% of the nominal strain. Thus, the stress in the X-axis direction and the strain in the Y-axis direction were controlled linearly. Numerical analysis increment was performed by three steps per process.

Stress $\boldsymbol{\sigma}_c$ at the end of forward loading process, elastic trial stress $\boldsymbol{\sigma}_d$ and the subloading surface state in the elastic trial step of the beginning of the inverse loading process are shown in Figure 7 (a). The subloading surface in the elastic trial step of the begginning of the inverse loading process re-expands after temporary contraction without passsing to the purely-elastic domain, as can also seen Figure 4.

The stress curves in the X- and Y-axis direction of two loading criteria are shown in Figure 7 (b, c). The subloading surface in the elastic trial step of the beginning of the inverse loading process re-expanded larger than the purely-elastic domain after once contracted. In this case, the elastic trial stress $\boldsymbol{\sigma}_d^{\text{trial}}$ was judged by the past loading criterion as the elastic loading process and numerical value was calculated as larger than the exact value (Figure 7 (b)). On the contrary, the rigorous loading criterion judged it as the plastic loading process. Moreover, the normal-yield ratio of the transition point where the subloading surface switched from contraction to re-expansion was applied to the initial value for the normal-yield ratio in the plastic corrector process. Therefore, the precise numerical analyses were performed using the rigorous loading criterion regardless of the stress directions.

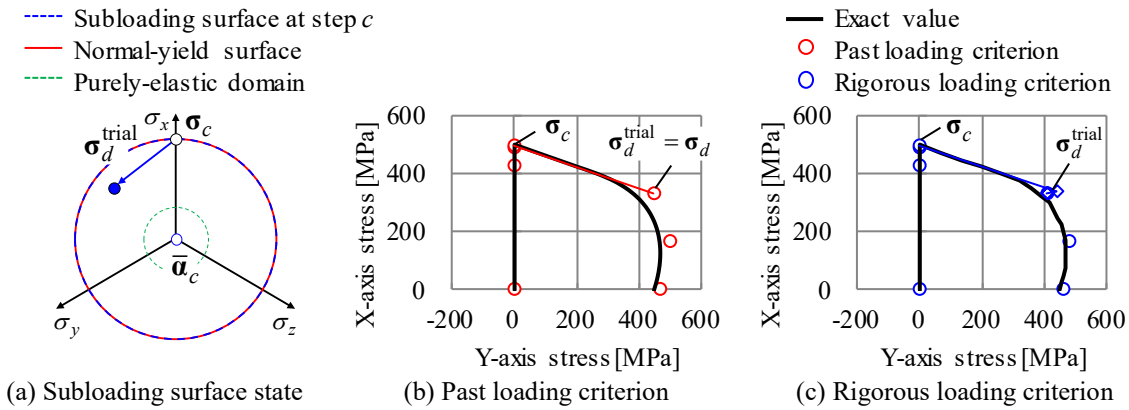

(a) Subloading surface state (b) Past loading criterion (c) Rigorous loading criterion

Figure 7: Bi-axial forward and inverse loading process, which the subloading surface in elastic trial step of beginning of inverse loading re-expand after once contraction.

4.2 Verification with error map

The error map was introduced to verify the accuracy of the past and rigorous loading criteria for various strain increments and directions. The elastoplastic deformation was applied up to 1% of the nominal strain in the X-axis direction, to produce the error map. Additionally, the stress σ^{num} was calculated using a series of strain increments corresponding to the elastic trial stress increments $\Delta\boldsymbol{\sigma}^{\mathrm{trial}}$.

$$\Delta\boldsymbol{\sigma}^{\mathrm{trial}} = \Delta\sigma_T\mathbf{T} + \Delta\sigma_N\mathbf{N} \tag{45}$$

Where, $\mathbf{N}$ and $\mathbf{T}$ are the normal and the tangential vector. In this study, to avoid division by zero, error equation is defined as the ratio of the exact value to the initial value for normal-yield surface.

$$\mathrm{Error} = \sqrt{\frac{(\sigma^{\mathrm{num}} - \sigma^{\mathrm{exact}}) : (\sigma^{\mathrm{num}} - \sigma^{\mathrm{exact}})}{F_0^2}} \times 100 \ [\%] \tag{46}$$

Where, σ^{exact} is the exact values calculated by the sufficiently small strain increment.

The error maps are shown in Figure 8. When the subloading surface was a forward loading state from 1% of the nominal strain, there was no difference in the judgement of loading process between the past and rigorous loading criteria. However, in inverse loading process, the numerical accuracy was different depending on the loading criteria. Because the past loading criterion can't consider the transition from contraction to expansion of the subloading surface,

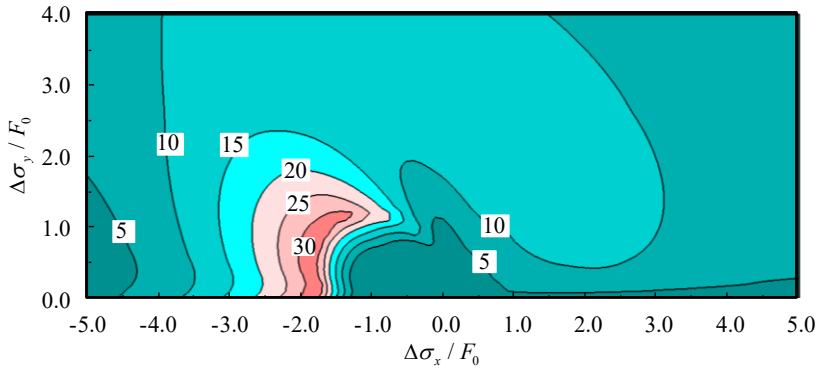

(a) Past loading criterion

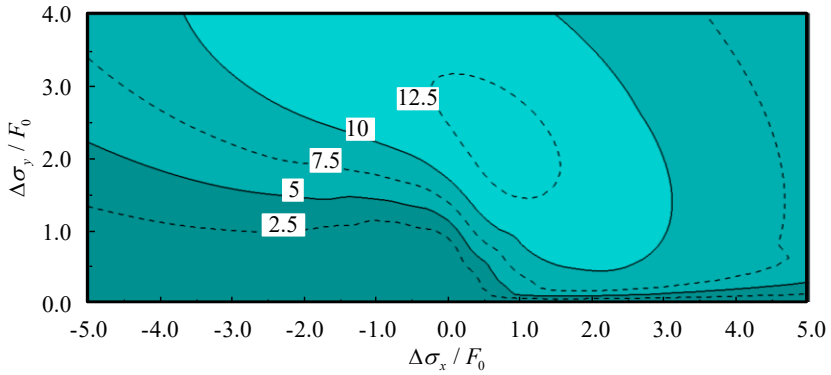

(b) Rigorous loading criterion

Figure 8: Error maps: numerical values in figures are error values (%).

the updated stress may be calculated as larger than the exact value. Conversely, the rigorous loading criterion can consider the process wherein the subloading surface re-expands after contraction. Therefore, the rigorous loading criterion can carry out more accurate numerical analyses compared to the past loading criterion.

5 CONCLUSIONS

- The rigorous loading criterion and the initial value calculation method for the normal-yield ratio for return-mapping were adopted to the complete implicit stress integration algorithm for the extended subloading surface model. Additionally, it has been formulated and implemented in ABAQUS through the user-subroutine UMAT.
- The rigorous loading criterion can represent that the plastic strain rate is induced when the subloading surface contracts in the elastic trial step if it once contracts but expands thereafter. The normal-yield ratio where the subloading surface switched from contraction to re-expansion is adopted to the initnial value for the plastic corector process in the general loading process. Therefore, the return-maping with the rigorous loading criterion and the initial value calculation algorithm for normal-yield ratio express accurate cyclic loading behavior in various directions.

REFERENCES

[1] Hashiguchi, K. Constitutive equations of elastoplastic materials with elastic-plastic transition, *J. Appl. Mech.* (1980) **47**:266-272.

[2] Hashiguchi, K. Subloading surface model in unconventional plasticity. *International Journal of Solids and Structures* (1989) **25**: 917-945.

[3] Yamakawa, Y., Hashiguchi, K. and Ikeda, K. Implicit stress-update algorithm for isotropic Cam-clay model based on the subloading surface concept at finite strains. *Int. J. Plasticity* (2010) **26**: 634–658.

[4] Hashiguchi, K. and Yamakawa, Y. *Introduction to Finite Strain Theory in Continuum Elasto-Plasticity.* John Wiley and Sons, (2012).

[5] Anjiki, T., Masanori, O., Koichi, H. Elastoplastic analysis by complete implicit stress-update algorithm based on the extended subloading surface model. *Transactions of the JSME (in Japanese)*. (2016) **82**: 839 DOI:10.1299/transjsme.16-00029.

[6] Fincato, R. and Tsutsumi, S. Closest-point projection method for the extended subloading surface model. *Acta Mechanica.* (2017) **228**:4213-4233.

[7] Iguchi, T., Fukuda, T., Yamakawa, Y., Ikeda, K. and Hashiguchi, K. An improvement of loading criterion for stress calculation based on return-mapping scheme for extended subloading surface plasticity model. *Journal of Applied Mechanics (JSCE)*. (2017) **20**:363-375 (in Japanese).

[8] Hashiguchi, K. *Foundations of Elastoplasticity: Subloading Surface Model.*, Springer, (2017).

[9] Simo, J. C. and Huges, T. J. R. *Computational Inelasticity*. Springer, (1998).

[10] Miehe, C. Numerical computation of algorithmic (consistetnt) tangent moduli in large-strain computational inelasticity, *Computational Methods in Applied Mechanics and Engineering*, (1996) **134**:223-240.